RSC Advances

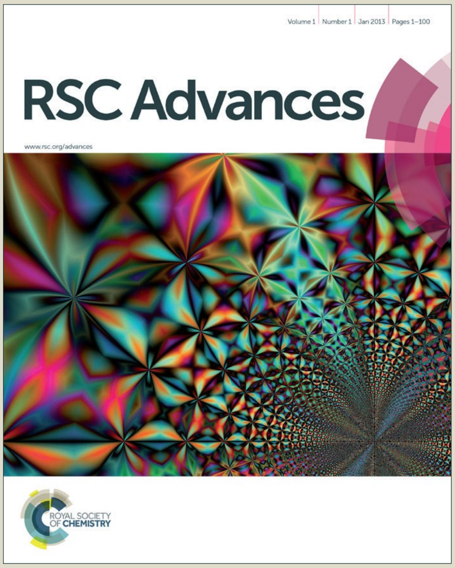

ROYAL SOCIETY OF CHEMISTRY

www.rsc.org/advances

A Novel High Conductive Ferroferric Oxide/Porous Carbon Nanofibers Composites Prepared by Electrospinning as Anode Materials for High Performance Li-ion Batteries

Shoupu Zhu, Ming Chen*, Jing Sun, Jingwen Liu, Tian Wu, Haiming Su, Shanshan Qu, Yongjuan Xie, Shishuang Wang, Xun Su and Guowang Diao*

College of Chemistry and Chemical Engineering, Yangzhou University, Yangzhou 225002, P. R. China

Key Laboratory of Environmental Materials & Environmental Engineering of Jiangsu Province, Yangzhou 225002, Jiangsu, P. R.China

Abstract: In this paper, ferroferric oxide (Fe_3O_4) nanoparticles/porous carbon nanofibers (Fe_3O_4/PCNFs) composites were successfully fabricated by elctrospinning and subsequent calcinations. The composites were characterized by X-ray diffraction, thermogravimetric analysis, scanning electron microscopy and transmission electron microscopy to analyze the structure, composition and morphology. The electrochemical performance was evaluated by coin-type cells versus metallic lithium. The results indicated that Fe_3O_4/PCNFs composites exhibited high reversible capacity and good capacity retention. The discharge capacity maintained 717.2 mA h g^{-1} at 0.5 A g^{-1} after 100 cycles. The excellent performances of Fe_3O_4/PCNFs composites are attributed to good crystallinity and uniformly dispersive Fe_3O_4 nanoparticles, and porous carbon shell with high conductivity. The carbon coating buffered the tremendous volumetric changes between Fe_3O_4 nanoparticles and Fe atoms in the charge/discharge processes and kept the structure integrity of Fe_3O_4 nanoparticles. Porous carbon nanofibers prepared by unique calcination process improved the conductivity of composites and provided free space for migration of lithium ions. The preparation of strategy is expected to be applied to the preparation of other transition metal oxides materials as

---

* Corresponding author. Tel.: +86 514 87975436; fax: +86 514 87975244. E-mail address: gwdiao@yzu.edu.cn (G. Diao), chenming@yzu.edu.cn (M. Chen).

superior anode materials for lithium-ion batteries.

Keywords: Porous nanofiber; Fe_3O_4 nanoparticles; Electrospinning; Hybrid anode materials; Li-ion battery

1 INTRODUCTION

Haze and greenhouse effect have become severe challenges to environment, which are closely connected to excessive use of fossil fuels [1-3]. Rechargeable lithium ion batteries are tools of energy exchange between chemistry energy and electric energy [3-4], which can store energy from clean energy [5]. As rechargeable lithium ion batteries have the characteristics of high energy density, long lifespan, environment friendly and fast charge-discharge rates [6-7], they have been widely applied to mobile phones, digital cameras and laptops, etc [7]. But hybrid electric vehicles and electric vehicles require Li-ion batteries to have higher energy density and rate capability [3,8] to match the performance of internal combustion vehicles [3].

Natural graphite seems to be the most promising candidate for the anode material in lithium-ion batteries because of its numerous advantages [9,10]. Graphite and graphitized carbon as anode materials in lithium-ion batteries have been used in many commercial products on the market [9]. Modification of carbonaceous anode materials which has been a research focus [11] can greatly improve materials' electrochemical performance. Composites of carbon nanomaterials and sulfides [12-16]/metal oxides [17-21] have been intensively studied for efficient energy storage. Transition metal oxides (MO) (Fe_2O_3, Fe_3O_4, NiO, CoO, Co_3O_4, Cu_2O, CuO, RuO_2 and Cr_2O_3 *etc.*) have much higher theoretical capacities (~1000 $mA\ h\ g^{-1}$) than graphite based on the conversion between MO and M [17]. But pure transition metal oxides as anodes in lithium ion batteries often have poor cycling performance owing to the collapse of lattice structure of the original crystal over several discharge/charge cycles as the tremendous volume changes [18-19]. A number of research methods about transition metal oxides as anodes in lithium ion batteries have been carried out to improve the deficiency and obtained excellent electrochemical performance by constructing nanostructured materials, hollow nanostructures, hybrid nanostructures, etc. Carbon coating is the most widely used modification techniques for transition metal oxides. On the one hand, carbon coating on the surfaces of metal oxide nanoparticles can reduce the side reactions of solid electrolyte interface (SEI) at the interface between metal oxide and electrolyte [19]. On the other hand, good electrical conductivity of carbon can make up for the poor conductivity of metal oxides and promote the electron transport. What's more, carbon coating as elastic buffer layers/supports [20] can confine the position of metal oxides and prevent the agglomeration and cracking of crystal structures which can enhance the cycle stability of electrode. In addition, nanostructured electrode materials have some special characteristics, such as large proportion of surface atoms, small size, etc. which lead to higher electrode/electrolyte contact area, shorter path lengths for Li^+ transport and higher charge/discharge rates[21]. So carbon coating nanostructured metal oxides as anodes in lithium ion batteries would strengthen the cycle stability and improve the high-rate charge-discharge performance. Iron oxides have the characteristics of low price, environment-friendliness and abundant resources, which make them charming anodes for high performance lithium-ion batteries [20].

A lot of Fe_3O_4/carbon nanocomposites [22-25] and Fe_2O_3/carbon nanocomposites [26-28] have been fabricated and detected as electrode materials for lithium ion batteries. Carbon coating iron oxides nanoparticles can form 0 D nanospheres [29-30], 1 D nanowires [31-32], 2 D nanoflakes [33-34] and 3 D structures of porous carbon foam loading iron oxide [35-36]. Electrospinning is one of the carbon coating methods and has been used to fabricate1 D hybrid carbon coating iron oxides nanofibers composites [37-41], 1 D iron oxides nanofibers [42-43] and 1 D carbon nanofibers for Li ion batteries [44-45]. The method can embed the iron oxides into a conductive carbon by subsequent heat treatment and enhance the electrochemical properties effectively. Zhang, X. [37] fabricated Fe_2O_3–carbon composite nanofibers as durable anode materials for lithium ion batteries. The cell exhibits a reversible capacity of 820 mA h g^{-1} at a current rate of 0.2 C even after 100 cycles. Chaudhari, S. [42] synthesized hollow-structured α-Fe_2O_3 nanofibers by a simple electrospinning technique and subsequent calcination at 500 ^oC for 4 h in air. The hollow fibers anodes obtained a high reversible capacity of 1293 mA h g^{-1} at a current density of 60 mA g^{-1} (0.06 C). Kim, C. [44] fabricated high-purity carbon nanofiber webs by combination of electrospinning 10 wt. % polyacrylonitrile (PAN) polymer - dimethyl formamide (DMF) solution and thermal treatments. Nanofiber webs thermally treated at 1000 ^oC in Ar have the highest reversible capacity of 450 mA h g^{-1} than that of 700 ^oC or 2800 ^oC at a discharge current density of 30 mA g^{-1}.

Here, 1D Fe_3O_4 nanoparticles/porous carbon nanofibers (Fe_3O_4/PCNFs) composites are fabricated by electrospinning a 10 wt. % PAN and 3 wt. % $Fe(acac)_3$ dissolving in DMF solution and subsequent thermal treatments (Fig. 1). The innovative thermal treatments are made up of four calcination processes for the first time. Firstly, the electrospun nanofibers were pre-oxidized at 250 ^oC in air to maintain their morphologies. Secondly, carbonization was proceeded at 1000 ^oC in argon to obtain high conductive graphitized carbon. Thirdly, oxidation was continued at 400 ^oC in blowed air to change Fe atoms and Fe C compounds into iron oxides and remove some graphitized carbon of the nanofibers to form pore structures. Carbothermic reduction was finally proceeded at 500 ^oC in Ar to change Fe_2O_3 nanoparticles into high conductive Fe_3O_4 nanoparticles with better crystal structures and further more increase porosity of the nanofibers. What should be noted is that the flow rate of air and calcinating equipment have very significant effects on content of carbon and types of iron oxides in the third calcination process. The excellent electrochemical properties of the novel high conductive Fe_3O_4/PCNFs composites anode is evident from the high capacity of

717.2 mA h g^{-1} after 100 cycles at 0.5 A g^{-1}.

2 EXPERIMENTAL SECTION

2.1 Fabrication of Fe_3O_4/PCNFs Composites

PAN with 150,000 average molecular weight was purchased from Aladdin. Analytic grade ferric acetylacetonate ($Fe(acac)_3$) and DMF were obtained from Sinopharm Chemical Reagent Co.,Ltd. All the reagents were not further purified before using.

In a typical process, 1 g PAN and 0.3 g $Fe(acac)_3$ were added into 8.70 g DMF and formed a 10 g mixture, followed by vigorous stirring at room temperature for at least 24 h. The obtained homogeneous dispersion was used as the Fe_3O_4/PCNFs composites precursor solution for electrospinning. The precursor solution was loaded into a 10 mL plastic syringe connected to a blunt-tip needle with a inner diameter of 0.33 mm. The distance between the needle tip and collector is 15 cm. The injection flow rate of the solution was set to 0.1 mm min^{-1} (about 1 mL h^{-1}) driven by a pumb. A total voltage power of 15 kV was applied between the needle (12 kV) and a plate (-3 kV) covered with aluminum foil. Electrospinning was proceeded with a commercial setup (Beijing Ucalery Technology Development Co., Ltd, SS-2535DC). The environmental humidity of electrospinning was 45±10 %, and temperature 25±5 °C. The electrospun nanofibers were firstly preoxidized at 250 ℃ for 120 min with a heating rate of 1 °C min^{-1} in air atmosphere in a tube furnace (Hefei Ke Jing Materials Technology Co., Ltd., OTF-1200xΦ50) to keep fibrous morphology, and then carbonized at 1000 ℃ for 120 min with a heating rate of 5 ℃ min^{-1} in argon atmosphere to obtain high conductive graphitized carbon. Then the composite nanofibers were calcined at 400 ℃ for 3 h with a heating rate of 5 ℃ min^{-1} in air atmosphere to obtain the Fe_2O_3 and Fe_3O_4 nanoparticle-loaded porous carbon nanofibers (Fe_xO_y/PCNFs) composites. It should be noted that the flow of air and the calcination time both have a profound influence on the compositions and morphology of the Fe_xO_y/PCNFs composites because it is likely that graphitized carbon is completely oxidized to CO_2 and Fe_xO_y transforms into pure Fe_2O_3 by much longer time calcination and bigger air flow rate at 400 ^{o}C in air. At last, Fe_3O_4/PCNFs composites were prepared by further calcination at 500 ℃ for 2 h with a heating rate of 5 ℃ min^{-1} in argon atmosphere.

For comparison, homogeneous dispersion containing 1.00 g PAN and 9.00 g DMF was also prepared, and then proceeded electrospinning and calcination with the same processes. In addition, the preoxidized nanofibers were calcined at 700 ^{o}C or 900 ^{o}C in Ar to observe electrical conductivity of calcinated nanofibers at different calcination temperature. For ease of description, the above products were renamed in this article as follows.

Table 1 Renaming of various products with different composition and calcination temperature.

Samples	$Fe(acac)_3$ g	PAN g	DMF g	Temp (atm) First	Temp (atm) Second	Temp (atm) Third	Temp (atm) Last
PAN0-250	0.00	1.00	9.00	250 ^{o}C (air)	—	—	—
PAN0-700	0.00	1.00	9.00	250 ^{o}C (air)	700 ^{o}C (Ar)	—	—
PAN0-900	0.00	1.00	9.00	250 ^{o}C (air)	900 ^{o}C (Ar)	—	—
PAN0-1000	0.00	1.00	9.00	250 ^{o}C (air)	1000 ^{o}C (Ar)	—	—
PAN0-400	0.00	1.00	9.00	250 ^{o}C (air)	1000 ^{o}C (Ar)	400 ^{o}C (air)	—
PAN0-500	0.00	1.00	9.00	250 ^{o}C (air)	1000 ^{o}C (Ar)	400 ^{o}C (air)	500 ^{o}C (Ar)
PAN3	0.30	1.00	8.70	—	—	—	—
PAN3-250	0.30	1.00	8.70	250 ^{o}C (air)	—	—	—
PAN3-1000	0.30	1.00	8.70	250 ^{o}C (air)	1000 ^{o}C (Ar)	—	—
PAN3-400	0.30	1.00	8.70	250 ^{o}C (air)	1000 ^{o}C (Ar)	400 ^{o}C (air)	—
PAN3-500	0.30	1.00	8.70	250 ^{o}C (air)	1000 ^{o}C (Ar)	400 ^{o}C (air)	500 ^{o}C (Ar)

Comment: Temp = Temprature, atm = atmosphere.

2.2 Materials characterizations

The crystal structures of as-prepared materials were characterized using powder X-ray diffraction(XRD) on a D8 Advanced with lynxEye and SolX (Bruker AXS, WI, USA) with a Cu-Kα radiation source between 10 ° and 80 °. The morphologies were characterized using a field-emission scanning electron microscopy (SEM) (S-4800Ⅱ, Hitachi, Japan） and a field emission transmission electron microscopy (TEM) (Tecnai 12, Philips, Holland) in the Test Center of Yangzhou University. A SEM (Zeiss Supra™ 55, Sapphire Carl Zeiss Group, Germany) and a TEM (JEM-2100, JEOL, Japan) in College of Chemistry and Chemical Engineering of Yangzhou University were also used to characterized the morphologies. High-resolution TEM (HRTEM) and high-angle annular dark-field scanning transmission electron microscopy (HAADF-STEM) were conducted using a FEI Tecnai G2 F30 STWIN (USA) operating at 200 kV. Thermogravimetric analysis (TGA) (Pyris 1 TGA, PerkinElmer, USA) was performed in air atmosphere up to 800 ^{o}C at a heating rate of 10 ^{o}C min^{-1}. Raman spectra was conducted with a laser Raman spectrometer (In Via, Renishaw, UK) at the 532 nm wavelength. The magnetic measurements of PAN3-400 and PAN3-500 were performed on a vibrating sample magnetometer (VSM) (EV7, ADE, USA). The electrical conductivities of different pure carbon nanofibers were measured by a direct volt-ampere method (SZT-2A, Suzhou Tong-Chang electronics company Ltd, CHN). Nitrogen physisorption–desorption measurements at 100 ^{o}C were performed by a surface area and porosity analyzer (ASAP 2020 HD88, Micromeritics, USA). Brunauer–Emmett–Teller (BET) analyses were done by software to characterize surface properties of porous carbon nanofibers. X-Ray photoelectron spectroscopy (XPS) measurements were conducted with an Al Kα (1486.8 eV) X-ray source (ESCALAB 250Xi, Thermo Fisher Scientific, USA).

2.3 Electrochemical measurements

The calcined flexible PAN0-500, PAN3-400 and PAN3-500 mats were cut into electrodes with size Φ16 mm, which were assembled into lithium ion batteries by attaching onto a current collector copper foil with 10 wt. % PVDF which dissolved in 1-methyl-2-pyrrolidone (NMP) as binder. The electrodes were first dried in a vacuum drying oven at 80 ^{o}C for 12 h. The PAN0-500, PAN3-400 or PAN3-500 electrode was about 2 mg. Then coin cells were assembled with metallic lithium as the counter/reference electrode, 1 M $LiPF_6$ in ethylene carbonate (EC), diethyl carbonate (DMC) and ethylmethyl carbonate (EMC) (1:1:1 by volume) as electrolyte, and Celgard 2400 polypropylene as separator in an high-purity argon-filled glovebox (VAC-Omni, OMNI-LAB, Vacuum atmospheres company, CA). Cyclic voltammetry (CV) measurements were performed using an electrochemical workstation (CHI660 E, Chenghua, CHN) at a scan rate of 0.0001 V s^{-1} between 0.01 and 3.0 V. Galvanostatic charge (lithium extraction) and discharge (lithium insertion) cycling of the cells were carried out using a battery test system (CT-3008W, Xinwei, CHN) at the different current densities of 0.05, 0.1, 0.2, 0.5 and 1.0 A g^{-1} between 0.01 and 3 V (*vs.* Li^+/Li) to observe ratio performance, and at the current density of 0.5 A g^{-1} to study cycle stability. Electrochemical impedance spectroscopic (EIS) measurements were carried out on an electrochemical analyzer (Autolab, Ecochemie, NL). All the current densities and capacities in this study were calculated on the basis of the weight of integral maps.

Finally, the morphology of PAN3-500 anode was observed by S-4800Ⅱ SEM and Tecnai 12 field emission TEM after 100 charge/discharge cycles at 0.5A g^{-1}.

3 RESULTS AND DISCUSSION

3.1 Preparation process

The overall synthesis procedures of Fe_3O_4/PCNFs composites are schematically illustrated in Fig. 1. PAN and $Fe(acac)_3$ were dissolved in DMF forming uniform viscous reddish-brown electrospinning solution by stirring 24 h. And electrospinning was carried out using above conditions in experimental section. The original electrospinning nanofibers (PAN3) films are yellow. Wide brown slices (PAN3-250) are obtained by pre-oxidation of PAN3 films at 250 °C in air. Black graphitized nanofibers (PAN3-1000) composites are prepared by calcination of PAN3-250 films at 1000 °C in Ar. Black porous graphitized carbon coating Fe_xO_y nanofibers (PAN3-400) sheets are gotten by calcinating PAN3-1000 at 400 °C in air. At last, black Fe_3O_4/PCNFs (PAN3-500) compounds are gained by calcinating PAN3-400 in Ar at 500 °C. The pieces have continuous macroscopic area shrinkages by pre-oxidation and graphitization, which can be demonstrated from the microscopic characterizations of SEM and TEM images below. PAN3-400 flakes have obvious weight loss and become more fluffy than PAN3-1000 pieces. A portion of carbon should be oxidized to CO_2 at 400 °C and form a large amount of pores in air atmosphere, which can be demonstrated by the BET results of PAN0-1000 and PAN0-400 as shown in Fig. 2.

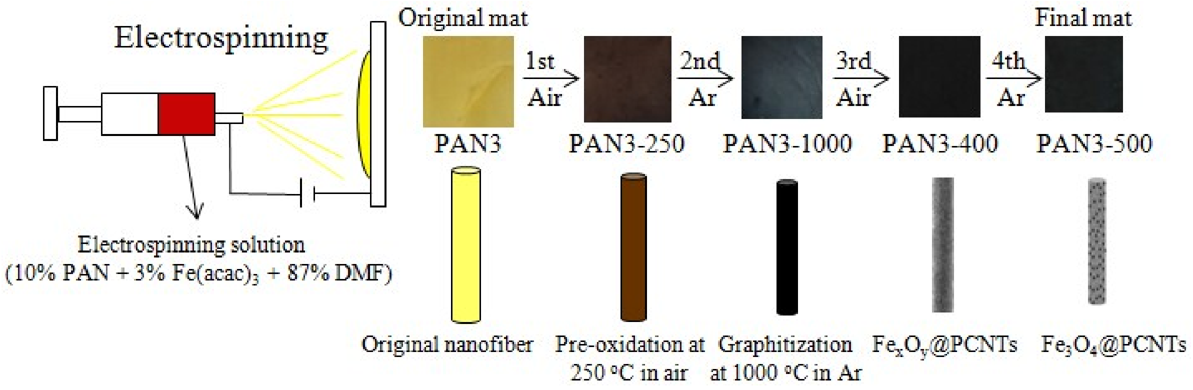

Fig. 1 Schematic illustration of the process of electrospinning and products of different calcination conditions.

3.2 Materials characterization

It is well known that high temperature is advantageous to the graphitization of nanofibers. The pure PAN0-250 was calcinated at the temperature of 700, 900 and 1000 °C under Ar. Table 2 shows the conductivities of carbon nanofibers with the various calcination temperatures and BET results of PAN0-1000 and PAN0-400. PAN0-1000 has the highest conductivity with the value of 476.2 $\mu S\ cm^{-1}$, which indicates that the graphitization degree increases with the carbonization temperature from 700 to 1000 °C. However, the GCNFs have small specific surface area. In order to increase the specific surface area of graphitized carbon nanofibers, the carbon nanofibers are continually calcinated at 400 °C under air atmosphere. Fig. 2(A) shows the nitrogen adsorption-desorption isotherms of PAN0-1000 and PAN0-400. The BET specific surface areas of PAN0-1000 and PAN0-400 are calculated to be 40.6 and 542.6 m^2 g^{-1}, respectively. After further calcination at 400 °C in air, the specific surface area of PAN0-400 increased 12.4 times than that of PAN0-1000. Fig. 2(B) displays the distributions of the pore size of PAN0-1000 and PAN0-400. Most pore diameter of PAN0-1000 ranges from 15 to 50 nm and a main peak centers at ~22 nm. The pore diameter of PAN0-400 has relatively large variation range of 3.5 – 50 nm. Most pore diameter of PAN0-400 ranges from 3.5 to 23 nm and a main peak centers at ~6.4 nm. As shown in Table 2, it is worth noting that the conductivity of PAN0-400 is also much higher than PAN0-250 calcinating at 700 °C (PAN0-700). The method will be applied in the preparation of the follow-up composite of nanofibers in this paper.

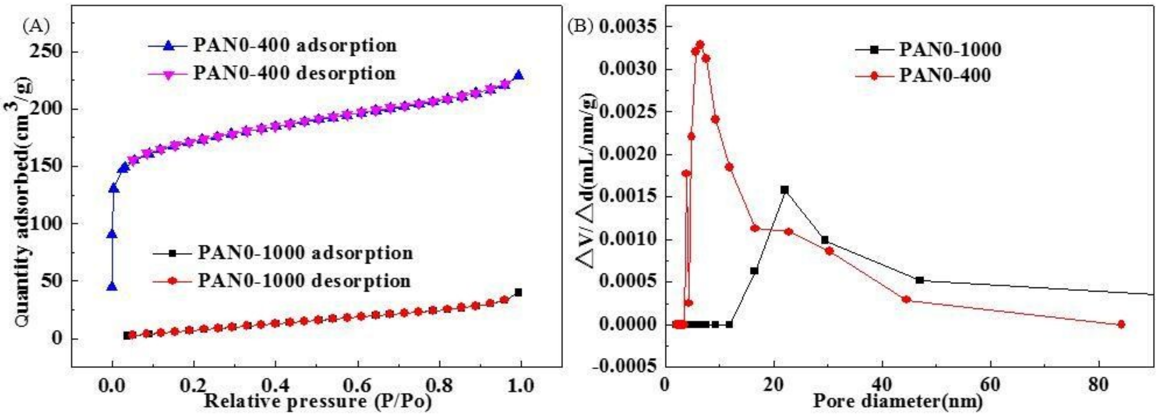

Fig. 2 Nitrogen adsorption-desorption isotherms of PAN0-1000 and PAN0-400 (A) and and pore size distributions of PAN0-1000 and PAN0-400 (B).

Table 2 Conductivity of carbon nanofibers in different calcinating process and BET test results.

Samples	PAN0-700	PAN0-900	PAN0-1000	PAN0-400
Conductivity (μS cm^{-1})	1.1	217.4	476.2	37.5
BET (m^2 g^{-1})	—	—	40.6	542.6

The morphology and the diameter of the electrospun nanofibers of PAN0 and PAN3 are compared. It is found that there is no distinct difference between pure PAN nanofibers and composite nanofibers as shown in Fig. S1, indicating that the electrospinning solution together with operation conditions of electrospinning in this experiment are appropriate to obtain uniform and perfect nanofibers. Fig. 3 shows SEM images of PAN3-250, PAN3-1000, PAN3-400 and PAN3-500. All nanofibers exhibit homogeneously distributed diameters. Fig. S2 shows the diameter distributions of PAN3-400 and PAN3-500. The mean sizes of PAN3-400 and PAN3-500 are 250 and 160 nm, respectively. More interesting, when the carbon nanofibers was successively calcinated at 500 ^{o}C under Ar atmosphere, the average diameter of PAN3-500 decreased obviously comparing with that of PAN3-400, which was due to the consumption of carbon in ferric iron reduction reaction. In the control experiment, the average diameter of PAN0-500 has no distinct decrease relative to that of PAN0-400 as shown in Fig. S3.

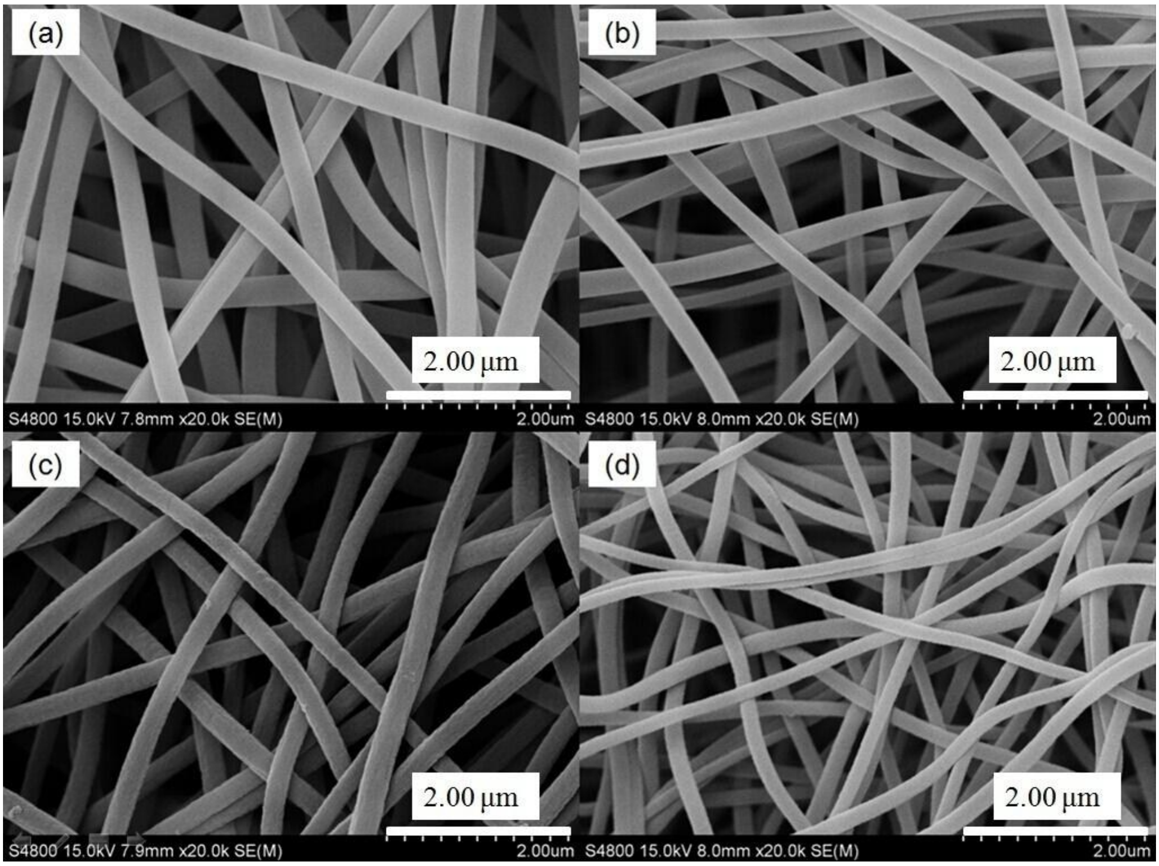

Fig. 3 SEM images of PAN3-250 (a), PAN3-1000 (b), PAN3-400 (c) and PAN3-500 (d).

As shown in Fig. 4(a) and (c), PAN3-400 and PAN3-500 have homogeneous morphologies. But the porosities are distinctly increasing along with continuous calcination. As can be seen from Fig. 4(b) and (d), there are many tiny pores and particles in PAN3-400 and PAN3-500. The portion of darker colour of PAN3-400 and PAN3-500 would be iron oxides nanoparticles. The lighter colour would be carbon and tiny pores of them. The little white spots should be pores. The above-mentioned iron oxides nanoparticles, carbon and pores can be certified by following XRD patterns in Fig. 8(A), Raman spectra in Fig. 8(E) and BET values in Table.2, respectively. What should be noted is that in the third calcination process, both the flow of air and the placed apparatuses of PAN3-1000 have great influence to integral morphology of nanofiber and respective content of carbon and iron oxides. Fig. S4 shows two differrent equipments in the third calcination process. Fig. 5 shows the SEM and TEM images of product calcinated using apparatus in Fig. S4(b) in the third calcinating process. Fig. 5(a) and Fig. 5(b) have obvious different morphologies comparing with Fig. 3(c) and Fig. 4(b), respectively. The degree contacting with air of PAN3-1000 in the third calcination process is responsible for the results. What’s more, large percentage shrinkage in area would occur or red brown product would generate at much higher temperature or larger flow rate of air. In this paper, the relevant experiments of a series of air flow and differrent equipments in the third calcinating process will not be further discussed. And all of the other products (PAN3-400 and PAN0-400) were calcinated using the apparatus in Fig. S4(a).

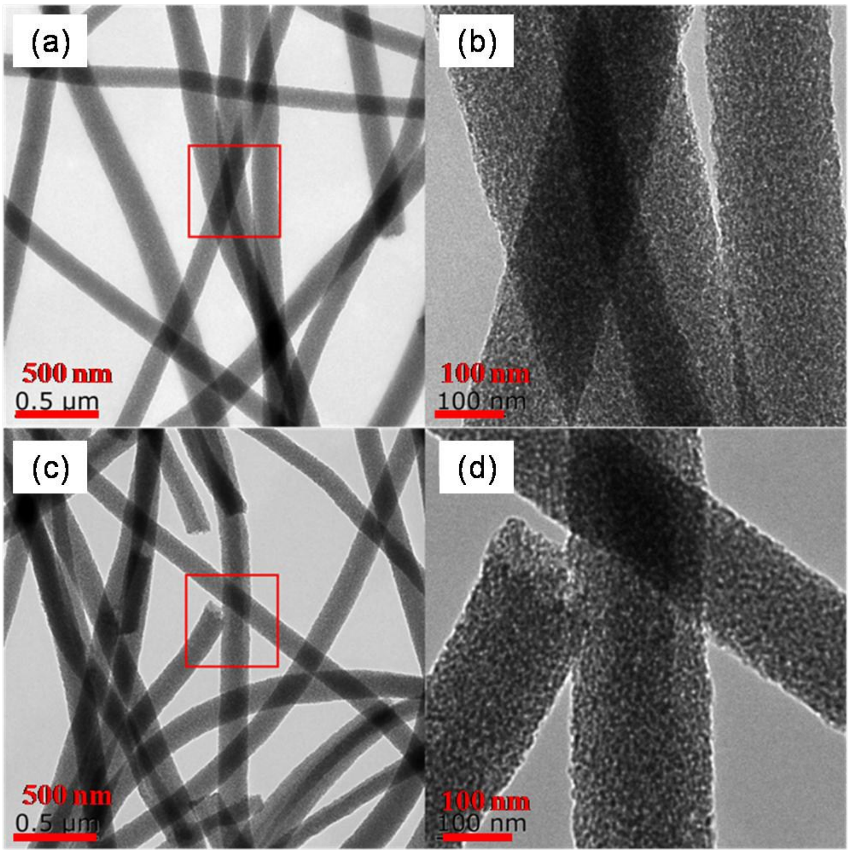

Fig. 4 Typical TEM image of PAN3-400 (a) and its partial magnification (b), representative TEM image of PAN3-500 (c) and its partial magnification (d).

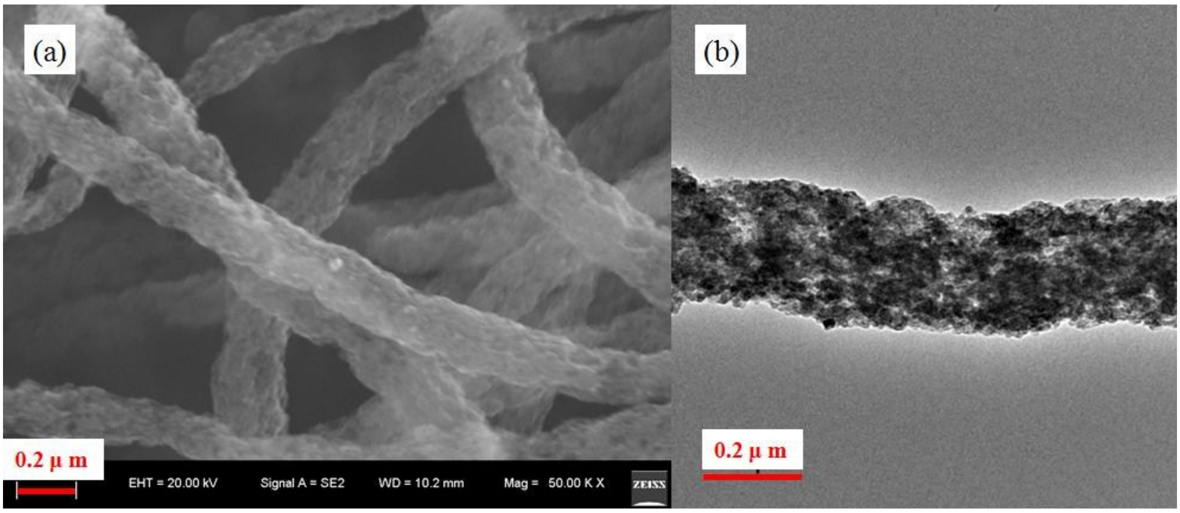

Fig. 5 SEM (a) and TEM (b) images of product using calcinating equipment in Fig. 4(b) in the third calcination process.

Fig. 6 shows HRTEM images of PAN3-500. The clear shell lattice fringes with d-spacing of 0.30 nm in HRTEM picture (Fig. 6(c)) shows are in good agreement with that of (220) plane of cubic Fe_3O_4. Fig. 6(d) demonstrates the clear shell lattice fringes with average d-spacing of 0.34 nm, corresponding to the (002) plane of hexagonal graphite. But the lattice structures are seldom observed. As shown in table 2, the conductivity of PAN0-400 is reduced significantly comparing with PAN0-1000. The lattice structures of graphitized carbon nanofibers would have been destroyed to a great extent in the calcination processes at 400 °C in air for 3 h and carbon thermal reduction at 500 °C for 2 h.

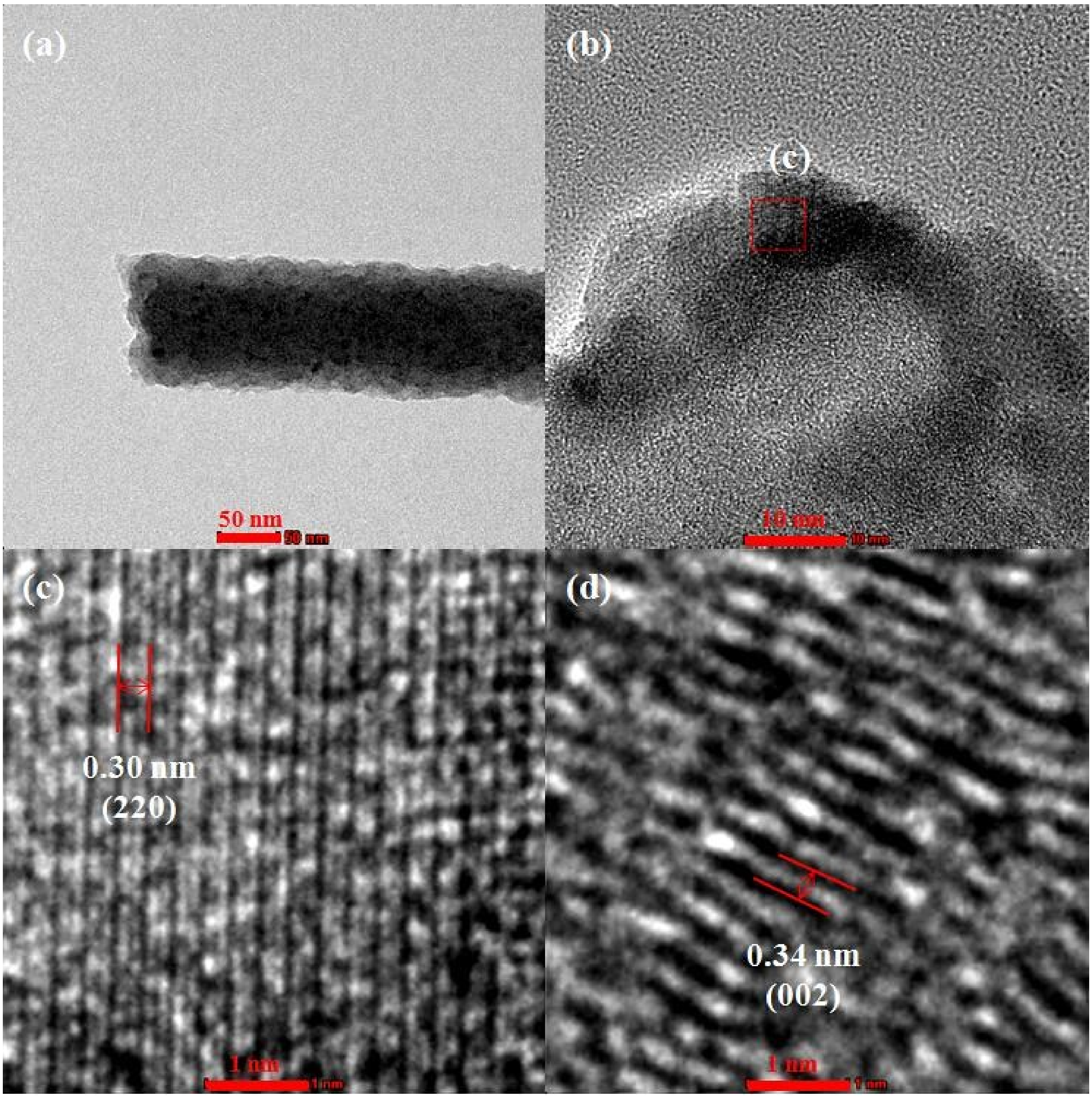

Fig. 6 Typical structure of PAN3-500 (a), partial enlargement of a cross-section of

PAN3-500 (b), the boxed region of part (b) - the observed crystallites in the HRTEM image corresponding to Fe_3O_4 (c), and seldom observed HRTEM image of lattice structure porous carbon of PAN3-500 (d).

The PAN3-500 composites are expressed by the element maps from EDX spectroscopy. The distributions of C, O and Fe are shown in Fig. 7(c), (d) and (e), respectively. The Fe and O elements prove the existence of iron oxide. All elements distribute uniformly in the nanofiber. Therefore, the element maps of EDX confirm the composition of PAN3-500 composites.

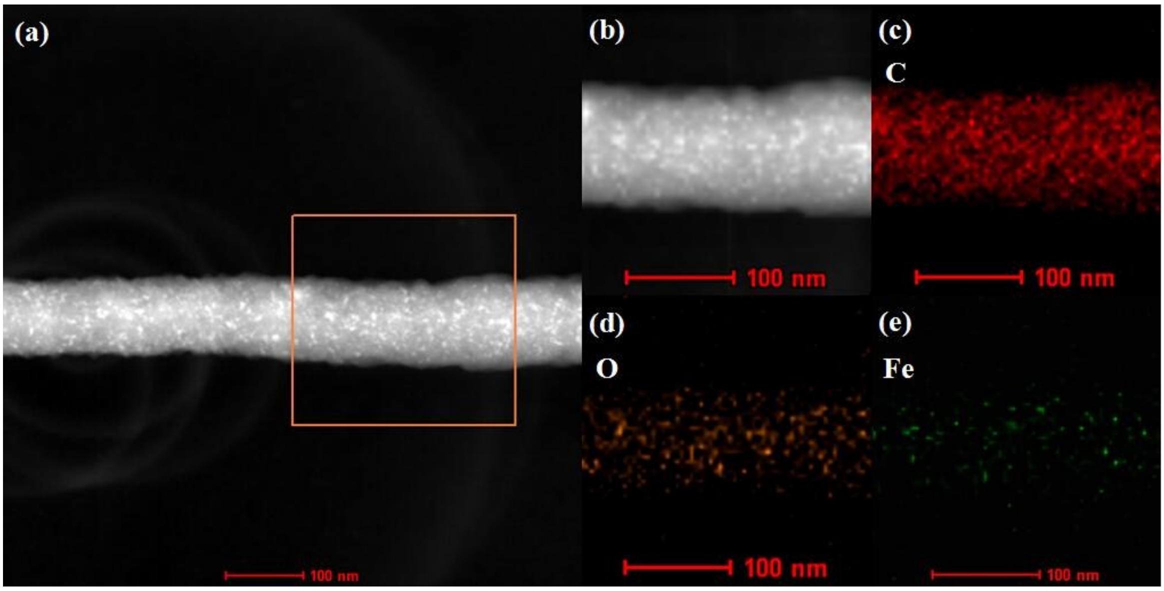

Fig. 7 HAADF-STEM images of PAN3-500 (a) and partial enlargement (b), element mapping of C (c), O (d) and Fe (e).

Fig. 8(A) shows the XRD patterns of PAN0-1000, PAN3-400 and PAN3-500. The identified diffraction peaks of PAN0-1000 nanofibers can be clearly assigned to the hexagonal graphite (JCPDS, card 41-1487). The peak at $2\theta = 26.38$ can be indexed to (002) lattice plane of hexagonal graphite, which manifests the precursor-PAN has changed into high conductive graphitic carbon. The peaks at $2\theta = 24.14$, 33.15, 35.61, 40.85, 49.48, 54.09, 62.45 and 63.99 can be indexed to (012), (104), (110), (113), (024), (116), (214) and (300) lattice planes of hexagonal Fe_2O_3 (JCPDS, card 33-0664), respectively. The peaks at 2θ = 18.27, 30.10, 35.42, 43.05, 56.94 and 62.52 can be indexed to (220), (311), (400), (511) and (440) lattice planes of cubic Fe_3O_4 (JCPDS, card 19-0629), respectively. In order to obtain the pure Fe_3O_4 in the nanofibers, PAN3-400 composites were calcinated at 500 ^{o}C in Ar. Under inert atmosphere, carbon is used as reductive agent and Fe_2O_3 transforms into Fe_3O_4. No impurity peaks from other iron oxide are observed, implying the high purity of Fe_3O_4 in the nanofibers. The intense diffraction peaks of Fe_3O_4 in PAN3-500 demonstrate the better crystal forms of Fe_3O_4 than that in PAN3-400. But the strong diffraction peak of graphitized carbon is disappeared in XRD patterns of PAN3-400 and PAN3-500, which indicates the structures of graphitized carbon have been destroyed to a great degree. The hysteresis curves of as-prepared PAN3-400 and PAN3-500 are shown in Fig. 8(B). The saturated magnetizations of PAN3-400 and PAN3-500 are about 15.0 and 29.2 emu g^{-1}, respectively. The results of hysteresis curves are consisted with their compositions shown by XRD results. The surface electronic state and composition of PAN3-500 were further investigated by XPS analysis as presented in Fig. 8(C) and (D). Fig. 8(C) reveals the existence of C, N, O and Fe elements in the PAN3-500. The existence of N of PAN3-500 in Fig. 8(C) should be attributable to nitrogen-containing groups of PCNFs originated PAN of the raw materials. Fig. 8(D) shows the high resolution of Fe 2p spectrum. The two main peaks located at 711.0 and 725.7 eV correspond to Fe 2p3/2 and Fe 2p1/2, respectively. The results shown the Fe^{3+} and Fe^{2+} states were coexisted in PAN3-500, which further confirmed the iron oxide in PAN3-500 is Fe_3O_4.

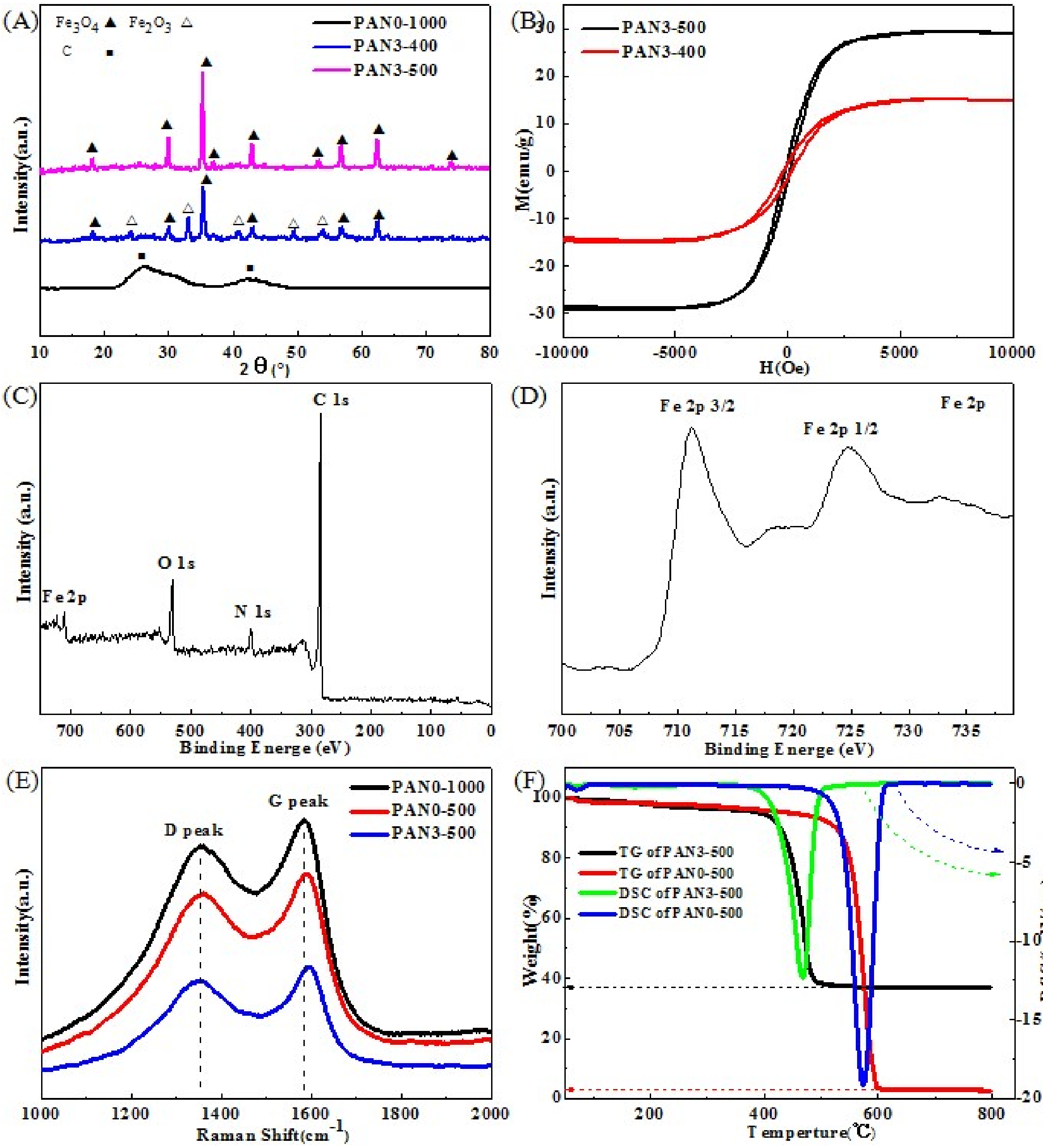

Fig. 8 XRD patterns of PAN0-1000, PAN3-400 and PAN3-500 (A), hysteresis loops of PAN3-400 and PAN3-500 (B), XPS survey spectrum of PAN3-500 (C) and high resolution of Fe 2p spectrum (D), Raman spectra of PAN0-1000, PAN0-500 and PAN3-500 (E), and TG-DSC curves of PAN0-500 and PAN3-500 (F).

Fig. 8(E) shows the Raman spectra of PAN0-1000, PAN0-500 and PAN3-500. All samples show strong D (disorder) peak at about 1360 $\mathrm{cm^{-1}}$ and G (graphite) peak at about 1590 $\mathrm{cm^{-1}}$. The intensity ratios R (I_D/I_G) of PAN0-1000, PAN0-500 and PAN3-500 are 0.96, 0.99 and 0.99, respectively. The large values of R indicate the degrees of disordered and defected carbon. From Fig. 8(F), the differential scanning calorimetry (DSC) and thermogravimetry (TG) curves of PAN0-500 indicate that the reaction is exothermic and the loss weight is mainly between 550 °C and 600 °C. But the TG curve of PAN3-500 reveals that the weight loss is mainly at the temperature range of 400 °C - 490 °C. It can be speculated that the graphitized carbon structures of PAN3-500 are destroyed more seriously than PAN0-500 due to the reaction of Fe_2O_3 and carbon etc. and the exothermic reaction of Fe_3O_4 oxidizing into Fe_2O_3 promotes the oxidation reaction of porous carbon at the lower temperature. The residual proportion of PAN3-500 is 36.9 wt. %. According to the results of TGA tests, the original percentages in weight of carbon and Fe_3O_4 in PAN3-500 are calculated to be 66.0 wt. % and 34.0 wt. %, respectively.

Electrochemical Performance

Porous carbon in the final mat PAN3-500 is sufficient to form a stable framework. So the PAN3-500 mat has very good flexibility, as shown in Fig. S5. The CV measurements were carried out to investigate the electrochemical reactions of PAN3-500 in the range of 3.0 to 0.01 V at a scan rate of 0.1 mV s^{-1} at room temperature. It is seen in Fig. 9(A) the PAN0-500 exhibits a cathodic peak at about 0.63 V which represents the formation of SEI film and the decomposition of the electrolyte [46] and two broad anodic peaks at about 1.16 V and 2.11 V attributing to irreversible reactions with electrolyte. In the subsequent cycles, the peak P2 at about 0.18 V and the peak P3 at about 0.25 V should be the insertion and extraction of lithium ion from the graphitized structures of porous carbon nanofibers, respectively. And the peak P1 at about 0.63 V disappears, indicating the stable and complete

SEI film has formed on the surface of carbon. As shown in Fig. 9(B), at the first cycle, PAN3-500 electrode exhibits a clear cathodic peak. The peak P1 at about 0.54 V might be the initial lithium insertion into the Fe_3O_4 to form $Li_2Fe_3O_4$, given by Eqn (1) [33,47] and the reduction reaction of $Li_2Fe_3O_4$ to Fe^0, along with the formation of amorphous Li_2O, given by Eqn (2), as well as the formation of SEI film [33,41,47] and the decomposition of the electrolyte. The peak P2 should be the extraction of lithium ion from the graphitized structures of porous carbon nanofibers and the peak at about 1.20 V should be irreversible reactions with electrolyte like as the peak at about 1.16 V of PAN0-500 in Fig. 9(A). The continuous broad peaks P3 and P4 at about 1.64 V and 1.82 V are the oxidation reactions of Fe^0 to Fe^{2+} and Fe^{2+} to Fe^{3+}, respectively [33,36,47]. The two electrochemical reactions of Fe^0 to Fe^{2+} and Fe^{2+} to Fe^{3+} owning nearby peak potentials and the irreversible reactions could be responsible for the phenomenon that the peaks P3 and P4 merged into a more broaden peak in the subsequent cycles. The total reaction is given by Eqn (3) [33,41,47].

$$Fe_3O_4 + 2\ Li^+ + 2\ e \rightarrow Li_2Fe_3O_4\ (1)$$

$$Li_2Fe_3O_4 + 6\ Li^+ + 6\ e \rightarrow 3\ Fe^0 + 4\ Li_2O\ (2)$$

$$3\ Fe^0 + 4\ Li_2O \rightarrow Fe_3O_4 + 8\ Li^+ + 8\ e\ (3)$$

EIS measurements were carried out at open circuit potential with an AC voltage amplitude of 5.0 mV in a frequency range from 100 kHz to 0.01 Hz to understand the electrochemical performance of PAN3-500 comparison with PAN3-400, PAN0-500 and PAN0-1000. Fig. 9(C) and (D) display the Nyquist plots of PAN3-500 and PAN3-400 electrodes, PAN0-1000 and PAN0-500 electrodes after 1 cycle at 0.5 A g^{-1}. From Fig. 9(C), the Nyquist plots of PAN3-500 and PAN3-400 have similar profiles, which are consisted of two semicircles, as well as a line, respectively. The two semicircles and the line from high frequency to low frequency were related to the resistance of SEI, charge-transfer resistance on the electrolyte/electrode interface and the solid-state diffusion resistance of Li ion in the electrode, respectively [13,15]. From Fig. 9(D), it clearly shows that the radius of the semicircle for PAN0-500 in the medium frequency region is much smaller than that of PAN0-1000, indicating the porous structured PAN0-500 has much lower electron-transfer resistance than graphitized PAN0-1000. The PAN3-500, PAN3-400 and PAN0-500 electrodes have remarkably small electron-transfer resistance compared with that of PN0-1000. The results indicates the greatly diminutive charge-transfer resistance at the electrode/electrolyte interface should be due to the porous structure in PCNFs of PAN3-500, PAN3-400 and PAN0-500, which can greatly improve the diffusion of lithium ions as well as the transfer of electrons for better elctrochemical performance [12-16].

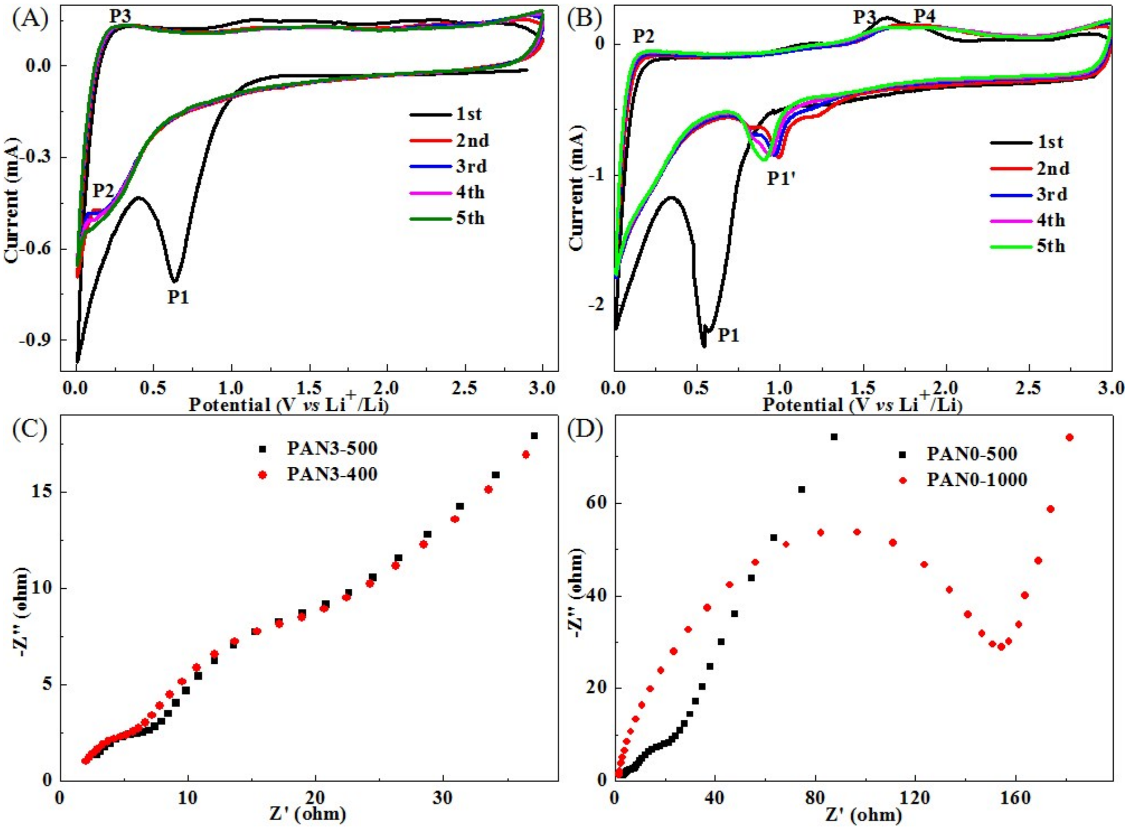

Fig. 9 CV measurements of PAN0-500 (A), PAN3-500 (B) cycled between 0.01 and 3 V at a scan rate of 0.1 mV s^{-1}, Nyquist plots of PAN3-500 and PAN3-400 (C), PAN0-500 and PAN0-1000 (D).

As the proportion of graphitized carbon in PAN3-500 is 66.0 wt. %, the specific capacitance of the composites is calculated as approximate 560 mA h g^{-1} based on the theoretical capacities of Fe_3O_4 926 mA h g^{-1} and graphite 372 mA h g^{-1}. Fig. 10(a) shows the charge-discharge cycle performance of PAN0-1000, PAN0-500, PAN3-400 and PAN3-500 at 0.5 A g^{-1} in the range of 3.0 to 0.01 V. In the 100th cycle, the discharge capacity of PAN0-1000, PAN0-500, PAN3-400 and PAN3-500 were 173.1, 261.1, 579.3 and 717.2 mA h g^{-1}, respectively. The test results show that the capacities of composite nanofibers are obviously higher than that of carbon nanofibers. The high capacity of PAN3-500 is attributed to superior porosity of porous carbon and carbon coating good crystallinity of Fe_3O_4. The discharge capacities of PAN3-500 in the 1st, 2nd, 10th, 30th, 50th, 70th and 90th cycles were 1422.1, 811.7, 672.9, 665.0, 674.6, 692.7 and 700.6 mA h g^{-1}, respectively, indicating that PAN3-500 had high capacity and remarkable capacity retention. The SEM images of PAN3-500 after 100 charge-discharge cycles and one discharge cycle are shown in Fig. 11. And the diameter distribution of PAN3-500 after 100 charge-discharge cycles and one discharge cycle is shown in Fig. S6. The mean diameter of PAN3-500 after 100 charge-discharge cycles and one discharge cycle is 180 nm. The results shows that the mean diameter of PAN3-500 after 100 charge-discharge cycles and one discharge cycle is the same as the original PAN3-500, which can demonstrate that PAN3-500 basically has no volume change in the charging-discharging process at the density of 0.5 A g^{-1}. The amounts of small pores which can afford space for inserted lithium should be responsible for this phenomenon. Fig. 10(b) shows the detailed charge and discharge curves of PAN3-500 at different cycle numbers. As shown in Fig. 10(c), the rate capabilities of PAN3-500 were investigated at various rates from 0.05 to 1.0 A $g^{−1}$ to further evaluate the electrochemical performance. When the densities were 0.05, 0.1, 0.2, 0.5 and 1.0 A $g^{−1}$, the PAN3-500 retained high specific capacities of 1050.6, 931.1, 857.0, 709.0 and 501.6 mA h $g^{−1}$ in their own 5th cycle, respectively. And then back to 0.1 A g^{-1}, the capacity still achieved 919.3 mA h g^{-1}. Fig. 10(d) shows the charge/discharge curves of PAN3-500 at different current densities, which display approximate symmetrical shape, indicating fine reversibility of Li$^+$ insertion/extraction.

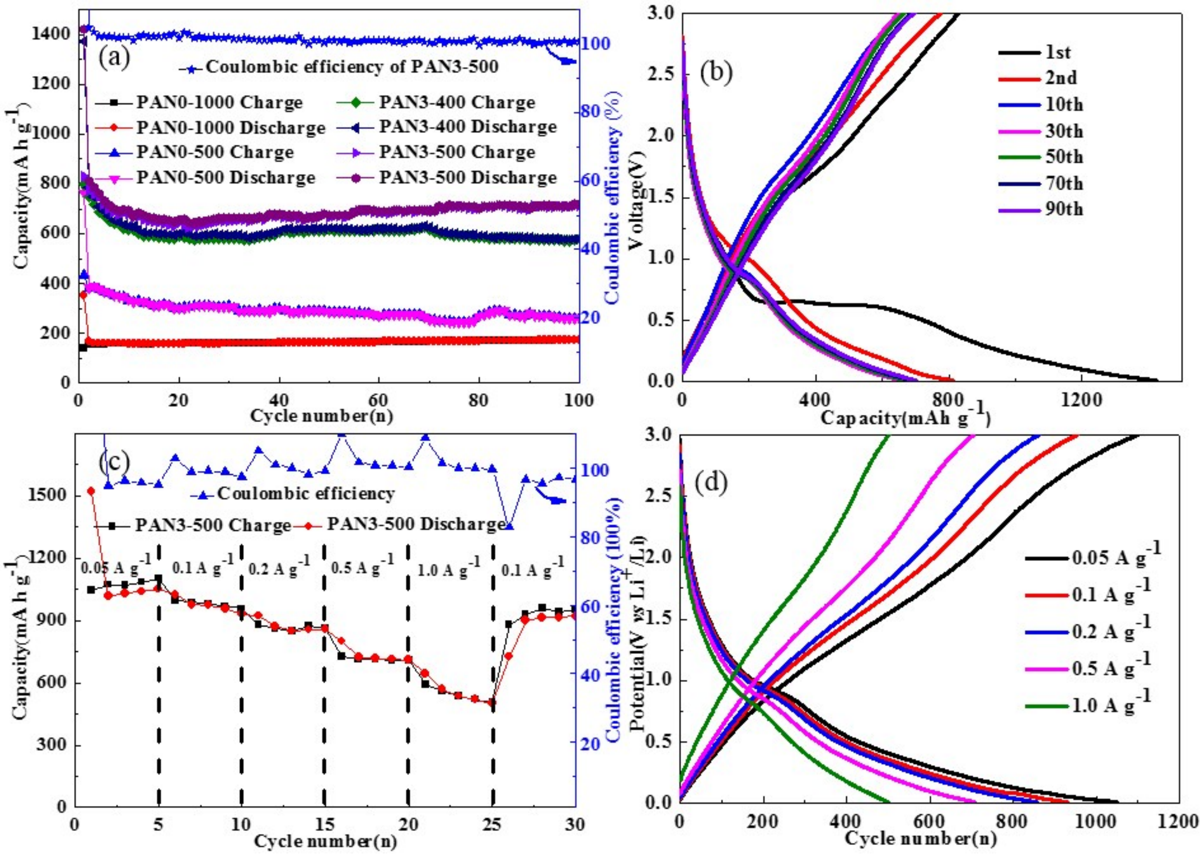

Fig. 10 The cycling performance of PAN0-1000, PAN0-500, PAN3-400 and PAN3-500 at a current density of 0.5 A g^{-1} (a) and relevant charge and discharge curves of PAN3-500 (b), charge-discharge performance of PAN3-500 at various current rates (c) and relevant charge and discharge curves (d).

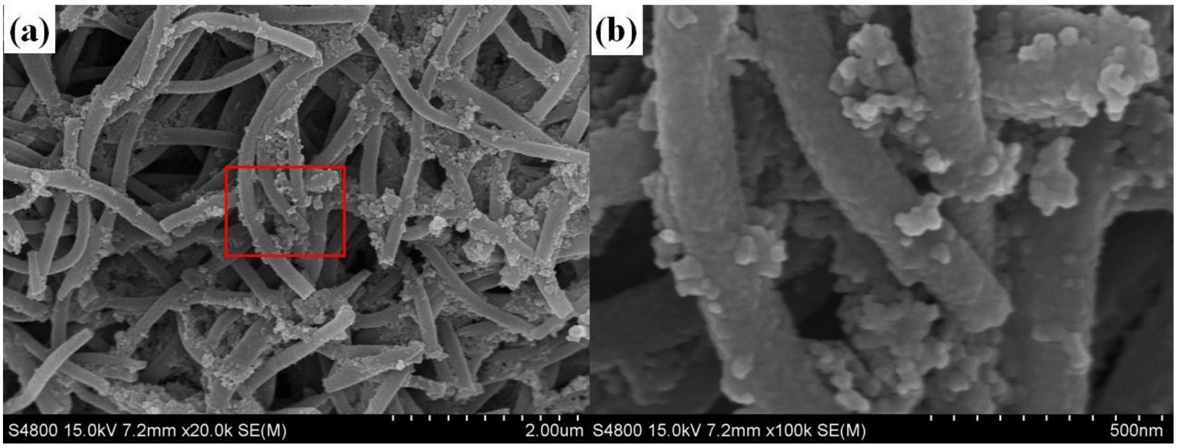

Fig. 11 SEM image of PAN3-500 after 100 charge-discharge cycles and one discharge cycle (a) and relevant magnifation (b).

It is worth noting that the electrochemical performance of PAN3-500 in this work are comparable to most of the electrospinning and calcined products, such as Fe_2O_3 nanofibers [42-43], carbon nanofibers [44-40] and iron oxides/CNFs composites [37-41] reported in previous literatures, as shown in Table 3.

Table 3 Comparison of the retaining capacity of Fe_xO_y nanofibers, carbon nanofibers or Fe_xO_y/CNFs composites preparing by electrospinning.

Nanocomposites	Precursors	Calcination temperature	Retaining capacity
Fe_2O_3-carbon	PAN-Fe(acac)$_3$	At 500 °C for 3h in air	820 mA h g^{-1} at 0.2 C [37]
α-Fe_2O_3-CNFs	PAN-$FeCl_3$	At 600 °C for 8 h in Ar	600 mA h g^{-1} at 50 mA g^{-1} [38]
α-Fe_2O_3 nanorods	PVP-Fe(acac)$_3$	At 500 °C for 5 h in air	1095 mA h g^{-1} at 0.05 C [39]
C/Fe_3O_4	PAN-Fe(acac)$_2$	At 600 °C for 10 h in Ar	1096 mA h g^{-1} at 0.2 A g^{-1} [40]
		At 700 °C for 10 h in Ar	300 mA h g^{-1} at 0.2 A g^{-1} [40]
Fe_3O_4@PCFs	PAN-PS-Fe_3O_4	At 600 ℃ for 2 h in Ar	541 mA h g^{-1} at 2.0 A g^{-1} [41]
Hollow Fe_2O_3 nanofibers	PVP-Fe(acac)$_3$	At 500 °C for 4 h in air	1293 mA h g^{-1} at 0.06 A g^{-1} [42]
Porous Fe_2O_3 nanotubes	PVP-Fe(acac)$_3$	At 500 °C for 3 h in air	987.7 mA h g^{-1} at 0.2 A g^{-1} [43]
Carbon nanofibers	PAN	At 700 °C in Ar	275 mA h g^{-1} at 0.03 A g^{-1} [44]
		At 1000 °C in Ar	450 mA h g^{-1} at 0.03 A g^{-1} [44]
		At 2800 °C in Ar	140 mA h g^{-1} at 0.03 A g^{-1} [44]
Carbon nanofiber	PAN	At 800 °C for 1 h in Ar	407 mA h g^{-1} at 0.15 A g^{-1} [45]
		At 1300 °C for 1 h in Ar	239 mA h g^{-1} at 0.15 A g^{-1} [45]
Fe_3O_4/PCNFs	PAN-Fe(acac)$_3$	At 1000 °C for 2 h in Ar,	
		at 400 °C for 3 h in Air,	579.3 mA h g^{-1} at 0.5 A g^{-1} [This]
		at 500 °C for 2 h in Ar	717.2 mA h g^{-1} at 0.5 A g^{-1} [This]

Comment: PS = polystyrene, PVP = polyvinylpyrrolidone, PCFs = porous carbon fibers.

CONCLUSIONS

In summary, we synthesized Fe_3O_4/porous carbon nanofibers by electrospinning and subsequent unique calcination processes. Graphitized carbon was obtained by calcination at 1000 °C in Ar. Porous structured carbon was obtained by further calcination at 400 °C in air, which had much higher porosity than graphitized carbon. Fe_3O_4/porous carbon nanofibers were prepared via the carbon-thermal reduction process by the final calcination at 500 ^{o}C in Ar. Porous carbon coating nano-sized Fe_3O_4 nanofibers composites had excellent performance as anodes for lithium ion batteries. The reversible capacity was higher than Fe_xO_y/porous carbon nanofibers composites and carbon nanofibers. Fe_3O_4/porous carbon nanofibers kept a reversible capacity of 717.2 mA h g^{-1} at 0.5 A g^{-1} after 100 cycles. At 0.05 A g^{-1}, the composites delivered a reversible capacity as high as 1050.6 mA h g^{-1}. The porous carbon nanofibers of coating Fe_3O_4 nanoparticles have good conductivity, which is useful for electronic transmission and fast diffusion of lithium in the charge-discharge process. What's more, carbon can buffer the volume changes between nano-sized Fe_3O_4 nanoparticles and Fe atoms in charging and discharging process and make the transition reactions in situ to maintain the crystal structures. So the combinations of conductive porous carbon nanofibers and nano-sized Fe_3O_4 are responsible for the higher capability and good cycling stability. We believe much higher capacity Fe_3O_4/porous carbon nanofibers can be fabricated by more appropriate calcination conditions containing calcinating apparatuse, temperature and flow rate of air. More importantly, the method of preparing Fe_3O_4/porous carbon nanofibers is novel.

ASSOCIATED CONTENT

Supporting Information

Additional experimental data including SEM images of PAN0 and PAN3, SEM images of PAN3-400 (a), PAN3-500 (c) and relevant diameter distributions of PAN3-400 (b), PAN3-500 (d), SEM images of PAN0-400, PAN0-500 and relevant diameter distributions, two differrent equipments in the third calcination process, picture of flexible PAN3-500 electrodes, SEM image of PAN3-500 after 100 charge-discharge cycles and one discharge cycle and relevant diameter distribution.

AUTHOR INFORMATION

Corresponding Author *E-mail: gwdiao@yzu.edu.cn, chenming@yzu.edu.cn. Tel.: +86-514-87975436. Fax:+86-514-87975244.

Notes

The authors declare no competing financial interest.

ACKNOWLEDGMENTS

The authors appreciate the Test Center of Yangzhou University for TEM and HRTEM measurements and the financial support from the National Natural Science Foundation of China (grant no. 21273195 and20901065), the Project Funded by the Natural Science Foundation of Education Committee of Jiangsu Province (12KJB150023), the Scientific Innovation Planing Program for Academic Graduates of Jiangsu Ordinary Universities (KYLX_1336), the Cooperation Fund from Yangzhou Government and Yangzhou University (Grant no. 2012038-9) and the Priority Academic Program Development of Jiangsu Higher Education Institutions.

References

[1] Ramanathan, V.; Carmichael, G. Global and Regional Climate Changes Due to Black Carbon. *Nature Geosci.*, 2008, **1**, 221-227.

[2] Ramanathan, V.; Feng, Y. Air Pollution, Greenhouse Gases and Climate Change: Global and Regional Perspectives. *Environ.*, 2009, **43**, 37-50.

[3] Thackeray, M. M.; Wolverton, C.; Isaacs, E. D. Electrical Energy Storage for Transportation-approaching the Limits of, and Going Beyond, Lithium-ion Batteries. *Energy Environ. Sci.*, 2012, **5**, 7854-7863.

[4] Dresselhaus, M. S.; Thomas, I. L. Alternative Energy Technologies. *Nature*, 2001, **414**, 332-337.

[5] Dunn, B., Kamath, H.; Tarascon, J. M. Electrical Energy Storage for the Grid: a Battery of Choices. *Science*, 2011, **334**, 928-935.

[6] Van Noorden, R. The Rechargeable Revolution: A Better Battery. *Nature*, 2014, **507**, 26-28.

[7] Scrosati, B.; Garche, J. Lithium Batteries: Status, Prospects and Future. *J. Power Sources*, 2010, **195**, 2419-2430.

[8] Kang, K.; Meng, Y. S.; Bréger, J.; Grey, C. P.; Ceder, G. Electrodes with High Power and High Capacity for Rechargeable Lithium Batteries. *Science*, 2006, **311**, 977-980.

[9] Yoshio, M.; Wang, H.; Fukuda, K.; Hara, Y.; Adachi, Y. Effect of Carbon Coating on Electrochemical Performance of Treated Natural Graphite as Lithium-ion Battery Anode Material. *J. Electrochem. Soc.*, 2000, **147**, 1245-1250.

[10] Yoshio, M.; Wang, H.; Fukuda, K.; Umeno, T.; Abe, T.; Ogumi, Z. Improvement of Natural Graphite as a Lithium-ion Battery Anode Material, from Raw Flake to Carbon-Coated Sphere. *J. Mater. Chem.*, 2004, **14**, 1754- 1758.

[11] Wu, Y. P.; Rahm, E.; Holze, R. Carbon Anode Materials for Lithium Ion Batteries. *J. Power Sources*, 2003, **114**, 228-236.

[12] Zhang, L. S.; Fan, W. and Liu, T. X. A Flexible Free-standing Defect-rich MoS_2/graphene/carbon Nanotube Hybrid Paper as a Binder-free Anode for high-performance Lithium Ion Batteries. *RSC Adv.*, 2015, **5**, 43130-43140.

[13] Miao, Y. E.; Huang, Y.; Zhang, L.; Fan, W.; Lai, F. and Liu, T. Electrospun Porous Carbon Nanofiber@MoS_2 Core/sheath Fiber Membranes as Highly Flexible and Binder-free Anodes for Lithium-ion Batteries. *Nanoscale*, 2015, **7**(25), 11093-11101.

[14] Zhang, L. S.; Huang, Y. P.; Zhang, Y. F.; Fan, W.; Liu, T. X. Three-Dimensional Nanoporous Graphene-Carbon Nanotube Hybrid Frameworks for Confinement of SnS_2 Nanosheets: Flexible and Binder-Free Papers with Highly Reversible Lithium Storage. *ACS Appl. Mater. Interfaces*, 2015, **7**(50), 27823–27830.

[15] Zhang, L. S.; Huang, Y. P.; Zhang, Y. F.; Gu, H. H.; Fan, W. and Liu, T. X. Flexible

Electrospun Carbon Nanofiber@NiS Core/Sheath Hybrid Membranes as Binder-Free Anodes for Highly Reversible Lithium Storage. *Adv. Mater. Interfaces*, 2016, DOI: 10.1002/admi.201500467.

[16] Zhang, L. S.; Fan, W.; Tjiu, W. W. and Liu, T. X. 3D Porous Hybrids of Defect-rich MoS_2/graphene Nanosheets with Excellent Electrochemical Performance as Anode Materials for Lithium Ion Batteries. *RSC Adv.*, 2015, **5**, 34777-34787.

[17] Poizot, P.; Laruelle, S.; Grugeon, S.; Dupont, L.; Tarascon, J. M. Nano-sized Transition-metal Oxides as Negative-electrode Materials for Lithium-ion Batteries. *Nature*, 2000, **407**, 496-499.

[18] Armstrong, M. J.; O'Dwyer, C.; Macklin, W. J.; Holmes, J. D. Evaluating the Performance of Nanostructured Materials as Lithium-ion Battery electrodes. *Nano Res.*, 2014, **7**, 1-62.

[19] Wu, H.B.; Chen, J.S.; Hng, H.H.; Lou, X.W. Nanostructured Metal Oxide-based Materials as Advanced Anodes for Lithium-ion Batteries. *Nanoscale*, 2012, **4**, 2526-2542.

[20] Zhang, L.; Wu, H. B.; Lou, X. W. Iron-oxide-based Advanced Anode Materials for Lithium-ion Batteries. *Adv. Energy Mater.*, 2014, **4**, 1032-1039.

[21] Arico, A. S.; Bruce, P.; Scrosati, B.; Tarascon, J. M.; Van Schalkwijk, W. Nanostructured Materials for Advanced Energy Conversion and Storage Devices. *Nature Mater.*, 2005, **4**, 366- 377.

[22] Zhu, T.; Chen, J. S.; Lou, X. W. Glucose-assisted One-pot Synthesis of FeOOH Nanorods and Their Transformation to Fe_3O_4@ Carbon Nanorods for Application in Lithium Ion Batteries. *J. Phys. Chem. C*, 2011, **115**, 9814-9820.

[23] Jin, S.; Deng, H.; Long, D.; Liu, X.; Zhan, L.; Liang, X.; et al. Facile Synthesis of Hierarchically Structured Fe_3O_4/carbon Micro-flowers and Their Application to Lithium-ion Battery Anodes. *J. Power Sources*, 2011, **196**, 3887-3893.

[24] Yoon, T.; Chae, C.; Sun, Y. K.; Zhao, X.; Kung, H. H.; Lee, J. K. Bottom-up in situ Formation of Fe_3O_4 Nanocrystals in a Porous Carbon Foam for Lithium-ion Battery Anodes. *J. Mater. Chem.*, 2011, **21**, 17325- 17330.

[25] Lee, J. E.; Yu, S. H.; Lee, D. J.; Lee, D. C.; Han, S. I.; Sung, Y. E.; et al. Facile and Economical Synthesis of Hierarchical Carbon-coated Magnetite Nanocomposite Particles and Their Applications in Lithium Ion Battery Anodes. *Energy Environ. Sci.*, 2012, **5**, 9528-9533.

[26] Zhou, G.; Wang, D. W.; Hou, P. X.; Li, W.; Li, N.; Liu, C.; et al. A Nanosized Fe_2O_3 Decorated Single-walled Carbon Nanotube Membrane as a High-performance Flexible Anode for Lithium Ion Batteries. *J. Mater. Chem.*, 2012, **22**, 17942-17946.

[27] Chou, S. L.; Wang, J. Z.; Wexler, D.; Konstantinov, K.; Zhong, C.; Liu, H. K.; et al. High-surface-area α-Fe_2O_3/Carbon Nanocomposite: One-step Synthesis and its Highly Reversible and Enhanced High-rate Lithium Storage Properties. *J. Mater. Chem.*, 2010, **20**, 2092-2098.

[28] Li, Y.; Zhu, C.; Lu, T.; Guo, Z.; Zhang, D.; Ma, J.; et al. Simple Fabrication of a Fe_2O_3/Carbon Composite for Use in a High-performance Lithium Ion Battery. *Carbon*, 2013, **52**, 565-573.

[29] Lv, P.; Zhao, H.; Zeng, Z.; Wang, J.; Zhang, T.; Li, X. Facile Preparation and Electrochemical Properties of Carbon Coated Fe_3O_4 as Anode Material for Lithium-ion Batteries. *J. Power Sources*, 2014, **259**, 92-97.

[30] Zeng, Z.; Zhao, H.; Wang, J.; Lv, P.; Zhang, T.; Xia, Q. Nanostructured Fe_3O_4@C as Anode Material for Lithium-ion Batteries. *J. Power Sources*, 2014, **248**, 15-21.

[31] Muraliganth, T.; Murugan, A. V.; Manthiram, A. Facile Synthesis of Carbon-decorated Single-crystalline Fe_3O_4 Nanowires and their Application as High Performance Anode in Lithium Ion Batteries. *Chem. Commun.*, 2009, **47**, 7360-7362.

[32] Wu, Y.; Wei, Y.; Wang, J.; Jiang, K.; Fan, S. Conformal Fe_3O_4 Sheath on Aligned Carbon

Nanotube Scaffolds as High-performance Anodes for Lithium Ion Batteries. *Nano Lett.*, 2013, **13**, 818-823.

[33] He, C.; Wu, S.; Zhao, N.; Shi, C.; Liu, E.; Li, J. Carbon-encapsulated Fe_3O_4 Nanoparticles as a High-rate Lithium Ion Battery Anode Material. *ACS Nano*, 2013, **7**, 4459-4469.

[34] Su, Y.; Li, S.; Wu, D.; Zhang, F.; Liang, H.; Gao, P.; et al. Two-dimensional Carbon-coated Graphene/metal Oxide Hybrids for Enhanced Lithium Storage. *ACS Nano*, 2012, **6**, 8349-8356.

[35] Yoon, T.; Chae, C.; Sun, Y. K.; Zhao, X.; Kung, H. H.; Lee, J. K. Bottom-up in situ Formation of Fe_3O_4 Nanocrystals in a Porous Carbon Foam for Lithium-ion Battery Anodes. *J. Mater. Chem.*, 2011, **21**, 17325-17330.

[36] Kang, E.; Jung, Y. S.; Cavanagh, A. S.; Kim, G. H.; George, S. M.; Dillon, A. C.; et al. Fe_3O_4 Nanoparticles Confined in Mesocellular Carbon Foam for High Performance Anode Materials for Lithium-ion Batteries. *Adv. Funct. Mater.*, 2011, **21**, 2430-2438.

[37] Zhang, X.; Liu, H.; Petnikota, S.; Ramakrishna, S.; Fan, H. J. Electrospun Fe_2O_3–carbon Composite Nanofibers as Durable Anode Materials for Lithium Ion Batteries. *J. Mater. Chem. A*, 2014, **2**, 10835-10841.

[38] Ji, L.; Toprakci, O.; Alcoutlabi, M.; Yao, Y.; Li, Y.; Zhang, S.; et al. α-Fe_2O_3 Nanoparticle-loaded Carbon Nanofibers as Stable and High-capacity Anodes for Rechargeable lithium-ion Batteries. *ACS Appl. Mater. Interfaces*, 2012, **4**, 2672-2679.

[39] Cherian, C. T.; Sundaramurthy, J.; Kalaivani, M.; Ragupathy, P.; Kumar, P. S.; Thavasi, V.; et al. Electrospun α-Fe_2O_3 Nanorods as a Stable, High Capacity Anode Material for Li-ion Batteries. *J. Mater. Chem.*, 2012, **22**, 12198-12204.

[40] Wang, L.; Yu, Y.; Chen, P. C.; Zhang, D. W.; Chen, C. H. Electrospinning Synthesis of C/Fe_3O_4 Composite Nanofibers and Their Application for High Performance Lithium-ion

Batteries. *J. Power Sources*, 2008, **183**, 717-723.

[41] Qin, X.; Zhang, H.; Wu, J.; Chu, X.; He, Y. B.; Han, C.; et al. Fe_3O_4 Nanoparticles Encapsulated in Electrospun Porous Carbon Fibers with a Compact Shell as High-performance Anode for Lithium Ion Batteries. *Carbon*, 2015, **87**: 347-356.

[42] Chaudhari, S.; Srinivasan, M. 1D Hollow α-Fe_2O_3 Electrospun Nanofibers as High Performance Anode Material for Lithium Ion Batteries. *J. Mater. Chem.*, 2012, **22**, 23049-23056.

[43] Wang, H. G.; Zhou, Y.; Shen, Y.; Li, Y.; Zuo, Q.; Duan, Q. Fabrication, Formation Mechanism and the Application in Lithium-ion Battery of Porous Fe_2O_3 Nanotubes Via Single-spinneret Electrospinning. *Electrochim. Acta*, 2015, **158**: 105-112.

[44] Kim, C.; Yang, K. S.; Kojima, M.; Yoshida, K.; Kim, Y. J.; Kim, Y. A.; et al. Fabrication of Electrospinning-derived Carbon Nanofiber Webs for the Anode Material of Lithium-ion Secondary Batteries. *Adv. Funct. Mater.*, 2006, **16**, 2393-2397.

[45] Peng, Y. T.; Lo, C. T. Effect of Microstructure and Morphology of Electrospun Ultra-small Carbon Nanofibers on Anode Performances for Lithium Ion Batteries. *J.Electrochem.Soc.*, 2015,**162**, A1085-A1093.

[46] Chen, M.; Yu, C.; Liu, S.; Fan, X.; Zhao, C.; Zhang, X.; Qiu, J. Micro-sized Porous Carbon Spheres with Ultra-high Rate Capability for Lithium Storage. *Nanoscale*, 2015, **7**, 1791-1795.

[47] Wang, J. Z.; Zhong, C.; Wexler, D.; Idris, N. H.; Wang, Z. X.; Chen, L. Q.; Liu, H.K. Graphene-encapsulated Fe_3O_4 Nanoparticles with 3D Laminated Structure as Superior Anode in Lithium Ion Batteries. *Chem.-Eur. J.*, 2011, **17**, 661-667.

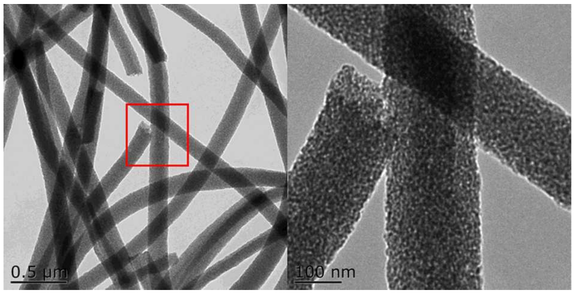

Ferroferric oxide/porous carbon nanofibers composites were synthesized by electrospinning and subsequent innovative thermal treatments, exhibiting enhanced electrochemical performance.